Probing surface dynamics of SIO_x thin-film electrodes during cycling through X-ray photoemission spectroscopy and operando X-ray reflectivity

Zijie Lu, Khawla Zrikem, Frédéric Le Cras, Masatomo Tanaka, Mitsunori Nakamoto, Anass Benayad, Samuel Tardif, Ambroise van Roekeghem

Probing Surface Dynamics of SiO_X Thin Film Electrodes during Cycling through X-Ray Photoemission Spectroscopy and *Operando* X-Ray Reflectivity

Zijie LU[1], Khawla ZRIKEM[2], Frédéric LE CRAS[2,3], Masatomo TANAKA[4], Mitsunori NAKAMOTO[4], Anass BENAYAD[2], Samuel TARDIF[1] and Ambroise VAN ROEKEGHEM[2,*]

[1] Université Grenoble Alpes, CEA, IRIG, 17 avenue des Martyrs, F-38054 Grenoble, France

[2] Université Grenoble Alpes, CEA, LITEN, 17 avenue des Martyrs, F-38054 Grenoble, France

[3] CNRS ICMCB UMR 5026, Univ. Bordeaux, Bordeaux INP, F-33600 Pessac, France

[4] Murata Manufacturing Co., Ltd., 1-10-1 Higashikotari, Nagaokakyo-shi, Kyoto, 617-8555, Japan

*Correspondance email : Ambroise.VANROEKEGHEM@cea.fr

Abstract

SiO_x electrodes are promising for high-energy-density lithium-ion batteries (LIBs) due to their ability to mitigate volume expansion-induced degradation. Here, we investigate the surface dynamics of SiO_x thin film electrodes cycled in different carbonate-based electrolytes using a combination of ex situ X-ray photoelectron spectroscopy (XPS) and *operando* synchrotron X-ray reflectivity analyses. The thin film geometry allows us to probe the depth-dependent chemical composition and electron density from surface to current-collector, through the solid-electrolyte interphase (SEI) and the active material, and the thickness evolution during cycling. Results reveal that SiO_x lithiation initiates below 0.4 V vs Li^+/Li, and indicate a close relationship between the SEI formation and SiO_x electrode lithiation, likely due to the high resistivity of SiO_x. We find similar chemical compositions for the SEI in FEC-containing and FEC-free electrolytes but a reduced thickness in the former case. In both cases, the SEI thickness decreases during delithiation due to the removal or dissolution of some carbonate species. These findings give insights

into the (de)lithiation of SiO_x, in particular during the formation stage, and into the effect of the presence of FEC in the electrolyte on the evolution of the SEI during cycling.

Keywords: SiO_x thin film electrodes, surface dynamics, lithium-ion batteries, X-ray photoelectron spectroscopy (XPS), *operando* synchrotron X-ray reflectivity (XRR), solid-electrolyte interphase (SEI).

1. Introduction

Since its commercialization by Sony in 1991[1], lithium-ion batteries (LIBs) have proven to be a reliable and high-performance energy storage system, widely used in portable electronic devices such as laptops, mobile phones, and other digital electronics. However, despite their use in electric vehicles (EVs), the required energy density for an EV to match the performance of internal combustion vehicles is 2-5 times greater than the energy offered by the state-of-the-art LIBs (~ 150 Wh/kg)[2]. To address this gap, substantial efforts have been devoted to developing active materials with higher energy density that are also naturally abundant and less expensive.

Si-based materials are considered among the most promising negative electrode materials for next-generation LIBs due to their high specific capacity up to ten times higher than that of the conventional graphite anodes (3579 mAh/g for $Li_{15}Si_4$ vs 372 mAh/g for LiC_6). However, the alloying process of Si and Li during lithiation causes a volume expansion of the electrode of *ca.* 300 %[3–5], which can lead to the cracking and pulverization of Si particles, eventually resulting in capacity fading[6,7]. In this context, silicon oxide-based electrodes (SiO_x, where $0 < x < 2$) are of particular interest since the O stoichiometry can mitigate the relative volume change after the first lithiation by forming irreversible products (*e.g.* Li_2O and Li_4SiO_4) that, in turn, can act as a buffering matrix to reversibly host the lithium insertion/deinsertion in Li_xSi_y[8,9]. Many studies have reported innovative syntheses of nanostructured SiO_x materials (nanoporous film[10], nanotube[11,12], composite[13]...), demonstrating promising electrochemical performance and cyclability of SiO_x-based materials[14]. Others focus on unraveling the irreversible and reversible processes[9,15] during cycling and providing a lithiation mechanism[16–19]. Nevertheless, only a few of them address the evolution of the SiO_x surface upon lithiation[20,21], in particular the formation and evolution of the solid electrolyte interphase (SEI) layer.

The formation and evolution of the SEI are key phenomena that influence the electrochemical performance, irreversible capacity and the cycle life of the battery. However, in the case of Si-based materials, the large and repeated volume changes occurring during cycling prevent the formation of a stable SEI layer and therefore the actual passivation of the negative electrode. Indeed, the large volume expansion of the Si anode generates cracks in the SEI and exposes fresh SEI-free areas to the electrolyte. This leads to continuous formation of SEI and capacity fading[19,22,23] due to both Li consumption and increase of the cell impedance. To improve the stability of SEI, introduction of electrolyte additives, such as vinylene carbonate (VC) and fluoro-ethylene carbonate (FEC)[24–26], was found to be beneficial. Specifically, Chao et al.[27] and Veith et al.[28] investigated the role of FEC in the improvement of the SEI forming on Si nanoparticles and amorphous Si thin films, respectively. To date there has been no published investigation using *operando* X-ray reflectivity (XRR) of the formation and evolution of SEI on SiO_x-based electrodes during cycling and on the role of electrolyte additives, up to our knowledge. Significant differences can be expected with respect to Si, in particular due to the lower conductivity and to the presence of irreversible products described above. Besides, the unambiguous characterization of the thickness and composition of the SEI and the tracking of their evolution upon cycling are challenging issues. Even under careful cell disassembly and electrode rinsing protocols, the structure and the chemical composition of the SEI can still be altered[29,30], which makes the precise characterization of SEI by *ex situ* techniques extremely challenging.

In recent years, synchrotron XRR has emerged as a powerful technique to investigate the electrode surface *in situ* and *operando*. The high flux of X-rays generated by a synchrotron facility allows one to perform fast XRR measurements during the cycling of flat, model electrodes, reflecting the processes taking place in a battery. Cao et al. investigated the lithiation mechanism of crystalline Si wafers by employing synchrotron XRR[31,32], revealing a layer-by-layer lithiation process and proposing a three-stage lithiation model. Additionally, they explored the dynamics of SEI formation at atomic scale through *operando* synchrotron XRR coupled with *ex situ* X-ray photoelectron spectroscopy (XPS)[33], highlighting that the SEI consists of two distinct regions. The top-SEI region was found to mainly contain LiF, while the bottom-SEI region was formed via the lithiation of the native oxide. The lithiation mechanism and SEI formation of amorphous Si deposited on Si substrate have been analyzed by *operando* neutron reflectometry. In particular, Jerliu

et al.[34] observed the expected volume change of the active material during cycling. Veith et al.[28] focused on the SEI itself, observing a thinner SEI when FEC was used as an additive. Surprisingly, it was observed that the SEI becomes thicker during delithiation and thins out again during lithiation in the absence of FEC, while the opposite was found with FEC. An important open question is whether the presence of additional oxygen in silicon suboxide-based (SiO_x) electrodes will modify these phenomena of formation and evolution of the SEI compared to the case of Si.

In this study, we aim at investigating the dynamics of surface modifications of SiO_x thin films electrodes during cycling in carbonate-based electrolytes with a focus on the role of additives on the SEI composition. This is in contrast to previous Si studies, in particular given the insulating nature of the relatively thick silicon oxide layer of interest. To achieve this, we combine *ex situ* XPS and *operando* XRR experiments on SiO_x (x~1) thin films to get a comprehensive record of the SEI formation at the surface of this active material. *Ex situ* XPS depth profiling measurements, conducted on samples prepared at different cut-off voltages, provide a chemical map of the electrode across its thickness, and an insight into its evolution as a function of the state of charge. Complementary to this, *operando* XRR measurements track in real-time the spatial modifications of the electrode surface with nanometer scale resolution during cycling. To fit the unique requirements of each technique, different sample setups were designed and different electrochemical cycling protocols were also employed, as detailed in the experimental section.

Through these complementary techniques, we aim to unravel the intricate processes governing surface modifications during cycling, shedding light on the SEI characteristics (thickness and composition) and the concomitant behavior of the SiO_x active material.

2. Experimental section

2.1 Sample preparation for XPS and XRR

The series of SiO_x thin film samples were prepared by RF magnetron sputtering of a $Si:SiO_2$ (1:1) composite target (2'' diameter, Neyco) under pure argon atmosphere, targeting a "SiO" film composition. This method was selected in preference to reactive sputtering of a pure Si target in $Ar:O_2$ atmosphere for sake of reproducibility. Samples were prepared in a Plassys PM300 deposition tool connected to an Ar-filled glove box, which allows to handle targets, substrates and thin film samples without any exposure to air. Three

positions are available for deposition in the chamber, which allows the preparation of three sets of samples in a row without opening the chamber. Depositions were carried out at a total pressure of 0.5 Pa, a power of 1.5 $W \cdot cm^{-2}$, a target-to substrate distance of 8 cm, an Ar flow of 20 sccm, and with no intentional heating of the substrate. In these conditions, the deposition rate was measured at 4.2 $nm \cdot min^{-1}$ by stylus profilometry. Therefore, a deposition time of 24 min was used to obtain 100 nm thick films. Before each series of depositions, the chamber was evacuated to a background pressure of less than $6 \cdot 10^{-7}$ Pa, filled with high purity argon (99.9999%), and the Si: SiO_2 target was then pre-sputtered during 1 h in the conditions described above.

For XPS *ex situ* experiments, SiO_x films (see corresponding Si 2p core-level peak results in supporting information (Figure S1)) were deposited on copper foil discs (14 mm in diameter x 0.01 mm thick). The experimental Si 2p spectrum is fitted using five pseudo-Voigt peak distributions, highlighting the oxidation states of silicon in SiO_x film. The presence of the different silicon oxidation states (Si^0 to Si^{4+}) is assigned to silicon surrounded with four silicon atoms, three silicon and one oxygen, two silicon and two oxygen, one silicon and three oxygen, and four oxygen (Si-Si, Si-(Si-O), Si-($Si-O_2$), Si-($Si-O_3$) and Si-($Si-O_4$)). At the surface of the film, the O/Si ratio is found to be about 1.4 (see supporting information).

The corresponding mass of SiO_x was in the range 48-52 µg. The oxygen-free (O < 5 ppm), soft-annealed, degreased copper foil with low roughness (Ra < 0.4 µm) was purchased from Schlenk Metallfolien. The XRR *operando* experiments required a much lower roughness, typically below 1 nm. Thus, the substrates for XRR were 1x1 cm^2 pieces of a 550 µm thick, phosphorus-doped Si (001) silicon wafer with a 2 nm thick chromium adhesion layer and a 200 nm thick copper layer coated on the back side for current collection.

2.2 Electrochemical protocol for *ex situ* X-Ray photoelectron spectroscopy

Samples to be characterized by XPS were conditioned electrochemically in 2032 coin cells, using the thin film sample as the positive electrode, a battery grade lithium foil as the negative one, a microporous polypropylene separator (Celgard 3200), and electrolyte in excess (200 µl). Two electrolytes were investigated with *ex situ* XPS: 1 M $LiPF_6$ in ethylene carbonate (EC): dimethyl carbonate (DMC) (15:85 weight %) and 1 M $LiPF_6$ in fluoro-ethylene carbonate (FEC): dimethyl carbonate (DMC) (15:85 weight %), labeled as

"EC/DMC" and "FEC/DMC", respectively. After assembly, the cells were placed in a temperature-controlled chamber at 25°C. The electrochemical sequence imposed to the cells comprised a stabilization step at a fixed potential (2 V vs Li^+/Li) for several hours, a voltage sweep at 5 $\mu V \cdot s^{-1}$ down/up to the targeted voltage and a final step with the target voltage imposed to avoid any voltage drift before dismantling the cell. Cell dismantling was carried out in an Ar-filled glovebox using a specific tool to prevent short-circuiting. Once removed from the cells, thin film electrodes were rinsed in fresh anhydrous DMC three times and left drying at room temperature. Finally, each sample was placed in a dry, airtight glass container for transfer to the XPS facility.

2.3 Ex-situ X-Ray Photoelectron Spectroscopy Measurements

The XPS measurements were performed using a Quantes spectrometer from Ulvac-PHI equipped with dual micro-focused monochromatic X-ray beam, Al Kα (1486.6 eV) and Cr Kα (5414.9 eV). In this study, we only used the Al Kα X-ray source with a beam diameter of 100 µm and 25 W of power. High-resolution spectral acquisition were performed using a pass energy of 69 eV, which corresponds to a resolution of 0.8-0.9 eV calculated from the full width at middle half (FWHM) of the Ag $3d_{5/2}$ peak. The survey was recorded with a pass energy of 280 eV, corresponding to a resolution of 1.8 eV. All XPS measurements were carried out in an ultrahigh vacuum chamber ($<7.10^{-10}$ mbar). The spectrometer was calibrated using the photoemission spectrum of gold ($Au4f_{7/2}$ = 84.0 eV, with reference to the Fermi level). The spectrometer is equipped with dual charge neutralization, however the XPS measurements were taken without the use of charge neutralization to avoid any lithium reactivity. All XPS spectra binding energies were corrected using the C1s line of carbon contamination (usually present at the surface of the sample) at 284.8 eV. The depth profiling was performed using 1 mm^2 raster Argon ion beam with an energy of 1 keV with steps of 1 min. A sputtering rate of 14.3 nm/min was measured in a reference SiO_x thin film with a thickness of 100 nm. In contrast, in a pure 25 nm thin SiO_2 layer, the sputtering rate was measured at 2 nm/min, indicating that the structure of our SiO_x thin film sample is significantly different from SiO_2.

The samples were deposited on a dedicated sample holder for XPS measurement and transferred from the Ar-filled glove box to the spectrometer through an air-protected transfer vessel to avoid air oxidation.

2.4 Electrochemical cell design and cycling protocol for *operando* X-ray reflectivity

Operando XRR measurements were performed on the BM32 beamline at the European Synchrotron Radiation Facility (Grenoble, France), using a 27 keV X-ray beam with a wavelength (λ) of 0.4592 Å. Throughout the XRR measurements, the incident angle (θ), representing the angle between the sample surface and the incident beam, was systematically adjusted from 0 to 2.5 degrees, while the detector angle, representing the angle between the detector and the incident beam, was correspondingly varied from 0 to 5 degrees.

The experimental set-up and the design of the *operando* electrochemical cell is shown in Figure 1 (a). The *operando* cell consists of stainless-steel flanges (top and bottom) and a polyether ether ketone (PEEK) body. The sample (Figure 1 (a) (3)) was fastened on the bottom flange with stainless steel screws and the Li metal was attached on the top flange. We used a half-cell with SiO_x thin film as the working electrode and Li as counter electrode. As in the XPS measurements, SiO_x electrodes were cycled in the EC/DMC electrolyte. However, due to the observed high roughness of the SiO_x electrodes cycled in the FEC/DMC electrolyte, an alternative electrolyte composition was employed to study the effect of FEC: 1 M $LiPF_6$ in ethylene carbonate (EC): dimethyl carbonate (DMC) : fluoro-ethylene carbonate (FEC) (15:70:15 weight %), labeled as "EC/DMC/FEC". During the *operando* XRR measurements, the cell was cycled in intermittent constant current mode that consists in applying current steps to reach the selected voltage values. For EC/DMC/FEC, the current density was 25 μA/cm², while, due to beam time constraints, EC/DMC was cycled at 50 μA/cm². The SiO_x electrode potential was held until two identical XRR curves were acquired consecutively to avoid any kinetic effects. At the end of the delithiation, the voltage was held at 2 V vs Li^+/Li for 2 h. Two XRR curves were measured respectively at the beginning and the end of this voltage plateau.

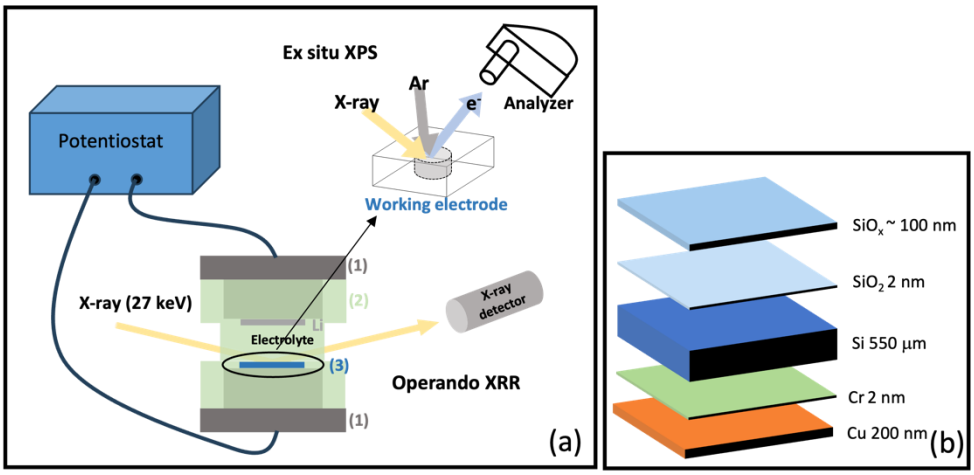

Figure 1. (a) Schematic of the experimental setup: (1) stainless steel, (2) PEEK cylindrical shell and (3) SiO_x working electrode. (b) Stacking of the SiO_x working electrode.

2.5 Principle of *operando* X-ray reflectivity

In an XRR experiment, one measures the specular reflection as a function of the incidence angle (θ), *i.e.* where the incidence angle is equal to the reflected angle. In this case, the momentum transfer q is perpendicular to the surface in z-direction ($q = q_z = \frac{4\pi sin\theta}{\lambda}$). The reflectivity curve obtained in the experiment is proportional to the square of the Fourier transform of the electron density gradient $\frac{d\rho_e}{dz}$ (Figure 2). Essentially, it provides information about the changes in electron density as a function of depth or position along the z-direction. In practice, to analyze the XRR curve, an electron density profile (EDP) in the z-direction $\rho_e(z)$ is initially built up by arbitrary layers, each characterized by variable parameters: thickness d_j and electron density ρ_{ej}. However, in real systems, the boundaries between these layers are not usually perfectly atomically flat, resulting in blurred interfaces. To account for this effect, a Gaussian distribution of the interface position is assumed and modeled by the Névot-Croce factor, which is mathematically represented as $e^{-q_z \sigma_j^2}$, with σ_j the Gaussian roughness. The corresponding XRR curve is then calculated and compared with the experimental curve. An iterative process is performed by varying the layers parameters until the calculated XRR curve closely matches the experimental one. Note that the bottom metal layers (Cr and Cu) of the Si substrate are too far from the surface to be probed in the XRR experiments. They are therefore disregarded in our analysis.

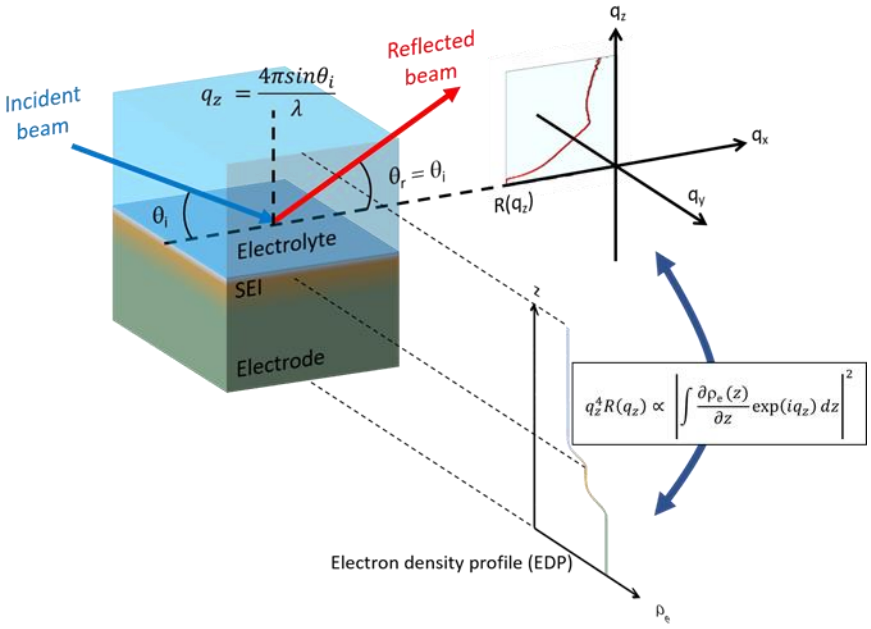

Figure 2. Principle of X-ray reflectometry.

3. Results and discussions

3.1 *Ex situ* XPS study

SiO_x // Li coin cells are cycled using a single sweep/cyclic voltammetry (CV) protocol (sweep rate 5 $\mu V \cdot s^{-1}$) and stopped at different cut-off voltages: 0.4 V, 0.15 V, 0.01 V (full lithiation) and 0.8 V (delithiation) vs Li^+/Li (Figure 3). For every cut-off voltage we cycled two coin cells, showing reproducible electrochemical curves, with minimal differences between the two groups, suggesting that they mainly reflect redox processes within the material. To minimize the effects of relaxation or surface reactivity, after cycling the cells are immediately disassembled in the glove box and washed with DMC for XPS analysis. The first reduction curve shows two main stages taking place in the 400-150 mV and 150-10 mV ranges respectively. Comparison of this curve with those obtained on amorphous Si thin films cycled in an all-solid system[35] or in a liquid electrolyte shows that the first stage involves a much greater charge transfer compared with the second stage than in the case of pure silicon. Furthermore, this stage seems to be the result of a single process, whereas in the case of Si, it is possible to distinguish two stages at this level, the first resulting from the reduction of oxidized silicon on the surface, followed by a second corresponding to an initial electrochemical alloying stage. There is therefore every reason

to believe that the stage taking place between 400 and 150 mV almost simultaneously involves the reduction of a majority fraction of the oxygen-bound Si within the material, followed by the transformation of the latter into a Li_xSi alloy. Once this transformation has taken place, the electrochemical behavior of the SiO_x electrode becomes very similar to that of Si, both for the rest of the reduction and during further delithiation, which takes place in two stages, the first between 10 and 350 mV, the second above 350 mV. Only a slight difference can be noticed on the curves related to EC/DMC compared the ones related to FEC/DMC at the early stage of the electrode reduction that is related to a step occurring around 0.8 V vs Li^+/Li.

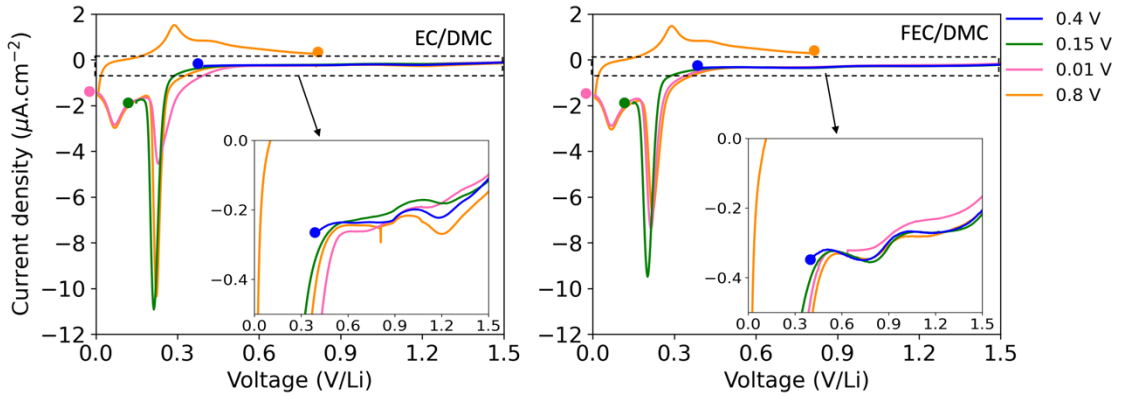

Figure 3. Cyclic voltammetry curves corresponding to the preparation of 4 samples conditioned in EC/DMC and in FEC/DMC 15:85 weight %, $LiPF_6$ 1M at 25 °C at different voltages: 0.4 V vs Li^+/Li (blue), 0.15 V vs Li^+/Li (green), 0.01 V vs Li^+/Li (pink) and 0.8 V vs Li^+/Li (orange).

3.1.1. Study of the effects of lithiation and delithiation processes on the internal composition and structure of resulting lithiated SiO_x (Li_zSiO_t-Li_xSi_y) thin films

Pristine and cycled thin film electrodes are characterized by XPS depth profiling, using fixed sputtering conditions. By examining the evolution of the Si 2p peak relative intensity as a function of the sputtering time (Figure 4), it is possible to follow the gradual changes in electrode thickness in both EC/DMC and FEC/DMC electrolytes.

In the early stage of reduction, at 0.4 V vs Li^+/Li, the thickness of SiO_x electrodes is unchanged compared to the pristine SiO_x reference electrode up to our experimental accuracy, for both electrolytes used. Then, the volume has clearly increased for electrodes stopped at 0.15 V vs Li^+/Li, *i.e.* after the first main electrochemical step at 0.2 V, since the sputtering time to remove all the lithiated SiO_x layer is estimated to ~13 minutes compared to 5 min for the pristine film. Electrodes cycled in EC/DMC and FEC/DMC exhibit a similar volume expansion. An initial delay of about 0.5 min is observed before the intensity of Si 2p starts to increase, which corresponds to sputtering of a thin layer composed of SEI

remnants. The swelling is even more significant at 0.01 V vs Li^+/Li, *i.e* after the second main electrochemical step at about 0.1 V, since the sputtering time to remove all the lithiated SiO_x has increased to ~18 min. Again, it is almost the same for the two electrolytes. The delay related to the SEI sputtering has also increased to ~ 2 min for FEC/DMC, which also suggests a noticeable thickening of the SEI compared to EC/DMC (~ 0.5 min) and constitutes the main difference observed between the two electrolytes. An estimation of the sputtering times and equivalent thicknesses is given in Supplementary Table S1. At the end of oxidation (0.8 V vs Li^+/Li), the thickness of SiO_x thin film electrodes, cycled in both electrolytes, decreases to ~ 240/260 nm. Therefore, the lithiation induce volume expansion of the thin-film electrode, which is only partially reversible during delithiation in the first cycle. Furthermore, the delay attributed to the SEI sputtering is much reduced (< 1 min), indicating a thinning of the surface layer upon delithitation. There is therefore a similarly partially reversible volume expansion of the SEI.

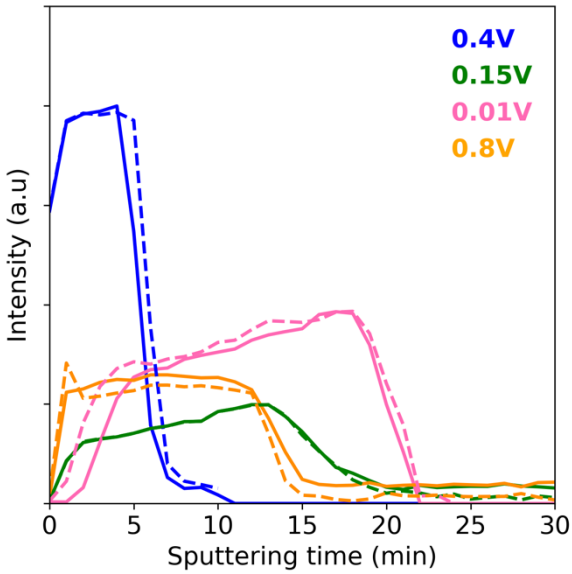

Figure 4. XPS Si 2p intensity depth profiling on SiO_x thin films electrodes cycled in EC/DMC (solid lines) and in FEC/DMC (dashed lines), and stopped at 0.4, 0.15, 0.01 (lithiation) and 0.8 (delithiation) V vs Li^+/Li.

To study the chemical composition of the internal structure of cycled SiO_x, we use the Si 2p XPS depth profiling spectra (Figure 5). In the pristine electrode, before the cycling process, the Si 2p peak is assigned to two main environments: Si-Si at lower binding energies (Si^0, ~ 99 eV) and a broad peak at higher binding energies assigned to oxidized silicon (Figure S1 in supporting information).

While cycling to 0.4 V vs Li^+/Li, the Si 2p peak shape does not change (Figure 5). However, upon lithiation below 0.4 V, the peak shape changes and the previous peak fitting

model, where peaks were explained by Si^0 and SiO_x contributions, does not apply any more. We assign the Si 2p region to two main contributions: Li_xSi_y at ~ 97 eV and Li_zSiO_t at ~ 101 eV (Figure 5). The Si 2p depth profile exhibits three stages: close to the top surface (interface with SEI), in the bulk of the electrode and at the bottom of the electrode, near the copper current collector (Figure 5). Since the XPS spectra were recorded without charge compensation to avoid lithium self-diffusion under electron flood-gun exposure, the Si 2p spectra are down shifted. Therefore, the spectra are shown without peak calibration and may show a small shift due to the varying chemical composition and electronic properties of the under-layers.

At 0.15 V and 0.01 V vs Li^+/Li, the Si 2p core level peaks beneath the SEI layer (Figure 5) in both electrodes still display two main contributions at ~ 97 and ~ 101 eV assigned to Li_xSi_y alloys and Li_zSiO_t silicates. The insertion mechanisms seem to be similar no matter the electrolyte (EC/DMC and FEC/DMC) used. This suggests that the electrochemical process at 0.2-0.25 V, indicated by the large current in CV (Figure 3), takes place at the same voltage as the first alloying step of pure *a*-Si thin films[35]. This reaction process combines: (i) cascading electrochemical conversion and alloying reactions leading to Li_xSi as a final product, and (ii) chemical reactions forming silicates. The onset of electronic transport through the SiO_x matrix is likely to be the trigger for this global step, and for the initiation of the SEI formation. The initial electronic conductivity of un-annealed SiO_x (x~1) thin film is indeed rather low, in the range of 10^{-9}-10^{-10} $S \bullet cm^{-1}$ which is 10^6 times lower than that of pure silicon. However, it can increase significantly as a function of the electric field[36,37]. The final reaction step during lithiation at ~ 0.1 V vs Li^+/Li leads to the formation of lithium-rich Li_xSi phases as in pure a-Si films, but this seems to take place also partly at the expense of the silicate matrix. At 0.01 V, the peak intensity related to Li_xSi alloys becomes higher than that of Li_zSiO_t near the electrode surface in contrast with the 0.15 V spectra, where the peak of Li_zSiO_t is higher than that of Li_xSi. This indicates that Li_xSi phases evolve as the lithiation proceeds, while the Li_zSiO_t phases remain. Previous studies suggest that such Li_xSi phases can grow in the Li_zSiO_t matrix. The detailed identification of Li_zSiO_t is out of the scope of this article, but based on the literature review, they should include Li_4SiO_6, $Li_6Si_2O_7$, Li_2SiO_3 and $Li_2Si_2O_5$[33,38–40]. We also note that close to the interface with the copper current collector, the signal attributed to lithiated oxide phases is enhanced. This means that the level of lithiation is different depending on

the distance from the electrode surface, reflecting the slow dynamics of Li diffusion in the SiO_x electrode and its heterogeneity across the thickness of the electrode.

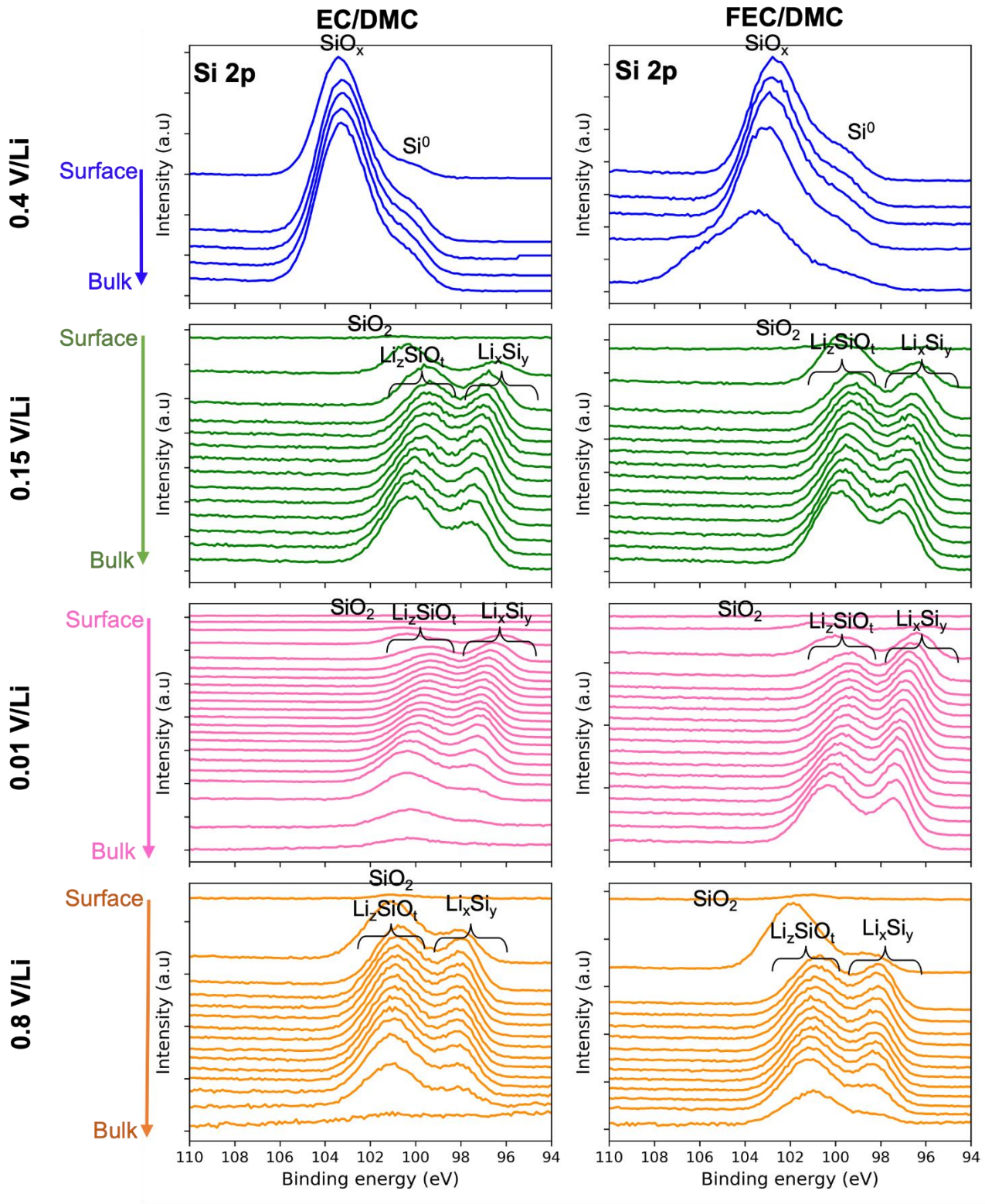

Figure 5. XPS depth profiling spectra of Si 2p core levels of SiO_x thin films electrodes cycled in EC/DMC and FEC/DMC and stopped at 0.4 V, 0.15 V, 0.01 V and 0.8 V vs Li^+/Li. The time interval between each curve corresponds to 1 min of

sputtering. Going from the top of the figure to the bottom corresponds to layers from the surface to the bulk, sometimes down to the current collector, at which a strong deformation or disparition of the spectrum can be observed.

Since the XPS probing depth is ~5 nm from the surface, the absence of intensity of the Si 2p spectra at the surface at 0.15 V and 0.01 V, and the low intensity at 0.8 V vs Li^+/Li, indicates the formation of a SEI whose thickness increases during lithiation and decreases during delithiation.

The chemical composition of the SEI formed at the surface of the electrodes cycled in EC/DMC and FEC/DMC is examined through the analysis of C 1s, F 1s and P 2p core peak depth profiling (Figure 6).

The sputtering rate of the SEI formed on the electrode surface differs from the sputtering rate of the bulk. After the lithiation process, the SEI sputtering rate is about 2 nm/min. This result is attributed to the structure and chemical composition of this layer, which is entirely different from that in the bulk.

Since we do not observe Si 2p peak at the top surface after lithiation at 0.01 V (Figure 4 and Figure 5) and no SEI related peak in the bulk of the electrode (Figure 6), we evidence that the SEI is constituted of a thin film located at the top surface of the electrode, without permeation into the bulk. This observation underscores the dense structure of the thin film electrode, affirming the absence of porosity during volumetric expansion.

3.2.2. SEI evolution upon lithiation and delithiation processes

Figure 6 shows a comparison between the evolution of C 1s, F 1s and P 2p core levels of SiO_x thin films cycled in EC/DMC and FEC/DMC and stopped at 0.01 V (fully lithiated) and at 0.8 V vs Li^+/Li (fully delithiated). Depth profiling analyses were conducted from the surface down to the first detected Li-(SiO_x) layer to gain insight into the structure of the SEI formed in both media. As mentioned in the experimental section, this study was performed without charge compensation, to avoid surface reactivity under electron or argon flood gun, used for surface charge compensation.

Figure 3 shows that there are two formation steps around 0.2 V and 0.08 V during lithiation. The XPS results at 0.4 V (SI Figure S2), 0.15 V (SI Figure S3) and 0.01 V (Figure 6) suggest significant changes in the SEI components at these formation potentials. At 0.4 V, a thin layer of LiF and free carbonate organic components were formed, then at 0.15 V

vs Li^+/Li, other organic components identified as alkyl-lithium carbonates (ROCOOLi) are formed (Figure S2 and Figure S3 in supporting information).

At 0.01 V vs Li^+/Li, the SEI formed at the electrode cycled in EC/DMC is constituted of LiF (F 1s peak at 685 eV), phosphates groups (PO_x like species at 133 eV) and a minor composition of lithium carbonates (as only a contamination carbon peak is detected at 285 eV). Similar compositions are seen in the electrode cycled in FEC/DMC, however, the amount of ROCOOLi and Li_2CO_3 is higher in this case[41–44]. This can be attributed to the decomposition of FEC by ring opening to form Li_2CO_3 and/or ROCOOLi. After one minute of sputtering, an increase of Li_2CO_3, LiF, and PO_x related species is revealed in the C 1s, F 1s and P 2p peaks at 290, 685 and 133 eV, respectively. These species result mainly from $LiPF_6$, salt decomposition to form LiF and phosphates groups and FEC and EC decomposition through bi-electronic process[45–47] forming Li_2CO_3. At this stage of the study, the decomposition kinetics of the salts and solvents are not trivial, but it appears that the SEIs have similar composition but slightly different thicknesses.

At 0.8 V vs Li^+/Li after delithiation, the SEI appears to be composed entirely of LiF and of free lithium carbonate organic components in the first 5 nm, which implies a partial dissolution of the SEI during the delithiation process.

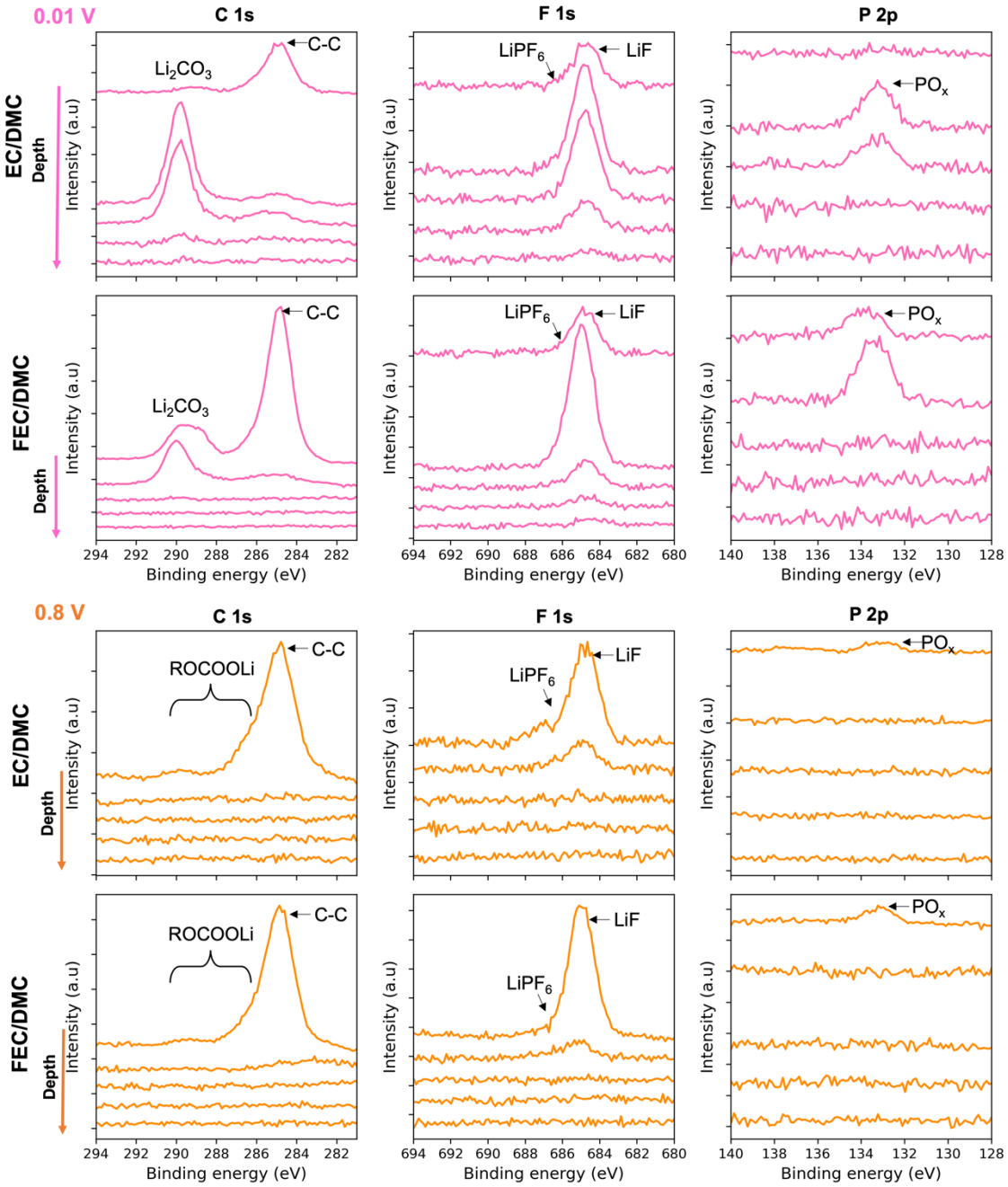

Figure 6. XPS depth profiling spectra of C1s, F1s, O1s and P2p of SiO_x thin films electrodes cycled in EC/DMC and FEC/DMC and stopped at 0.01 V vs Li^+/Li (pink lines) and at 0.8 V vs Li^+/Li (orange lines). The time interval between each curve corresponds to 1 min of sputtering.

In summary, the XPS depth profiling analysis of the SiO_x thin films at different voltages revealed a partially reversible volume expansion in the SiO_x electrode cycled with two different electrolytes. The lithiation process transforms the chemical composition from SiO_x to a combination of Li_tSiO_z and Li_xSi_y, persisting through delithiation with a proportional evolution.

Despite expectations from literature associating the addition of FEC with the formation of a more robust SEI, decomposed from FEC into LiF and polymeric FEC[27,28,48], our XPS results show similar SEI compositions in EC/DMC and FEC/DMC. This could be linked to our observation that SEI formation initiates only below 0.4 V vs Li^+/Li for both EC/DMC and FEC/DMC electrolytes, likely due to the insulating behavior of the thin film before lithiation. On the other hand, aligning with another reported influence of FEC, our results indicate a thinner SEI in FEC/DMC-based electrolyte[25]. This aligns with the notion that polymeric FEC species enhance SEI flexibility[49], preventing cracks and hindering excessive growth[28].

While providing valuable insights into the evolving chemical compositions of SiO_x and SEI during cycling, the XPS results raise questions about the specific effects of FEC. To delve deeper into the structural evolution of the SiO_x electrode and to unravel the dynamics of the SEI forming on the active material, particularly regarding the influence of FEC, we performed *operando* XRR measurements. This technique uniquely offers real-time, atomic-scale resolution of spatial modifications on the electrode surface during cycling, without the need of dismantling the cell and rinsing the electrode, allowing us to address these questions and gain a more comprehensive understanding of the surface evolution of SiO_x thin films during cycling.

3.2 Results of *operando* XRR

3.2.1 Fitting models of XRR data

The XRR curve of pristine SiO_x electrode in the EC/DMC-based electrolyte at open circuit voltage (OCV) is presented in Figure 7 (a). It exhibits distinct oscillations in the range of 0.03 $Å^{-1}$ to 0.08 $Å^{-1}$, which are known as Kiessig fringes. These fringes arise due to the constructive and destructive interference of X-rays partially reflected from two distinct interfaces: the SiO_x/electrolyte and the SiO_x/substrate interface. The Kiessig fringes can provide essential structural characteristics of the probed layer. The width of these fringes indicates the thickness of the probed layer. In this case, the thickness of the SiO_x layer can be estimated by the formula $d = \frac{2\pi}{\Delta q}$, resulting in a value of 103 nm, close to the nominal value. Moreover, their form and amplitude are indicative of the electron density contrast between the probed SiO_x layer and its adjacent layers. The asymmetry and the low amplitude of these Kiessig fringes suggest an inhomogeneity of the SiO_x layer. This observed inhomogeneity in the SiO_x matrix may arise from the presence of different (nano-)domains, as evidenced in the Si 2p XPS spectrum of the pristine SiO_x electrode

(Figure S1), where distinct peaks corresponding to Si-Si and SiO_2 were identified. Consequently, a four-layer model was employed to fit the XRR curve of the pristine SiO_x electrode at OCV, as illustrated in Figure 7. The XRR data and the fit-derived electron density profile (EDP) are depicted in Figure 7 (a) and (b), respectively. Proceeding from the Si wafer to the electrolyte, the four layers of the model are: a native oxide layer, denoted as "SiO_2", two intermediate oxide layers, labeled as "SiO_x-1", "SiO_x-2", and a "bulk SiO_x" layer. We note that a rapid variation of the oxygen content in SiO_x in the vicinity of the current collector is also suggested from the XPS results. Detailed rationalization for this fitting model is available in the supporting information. Similarly, for the EC/DMC/FEC based electrolyte, we used the same four-layer model to fit the XRR curve at OCV.

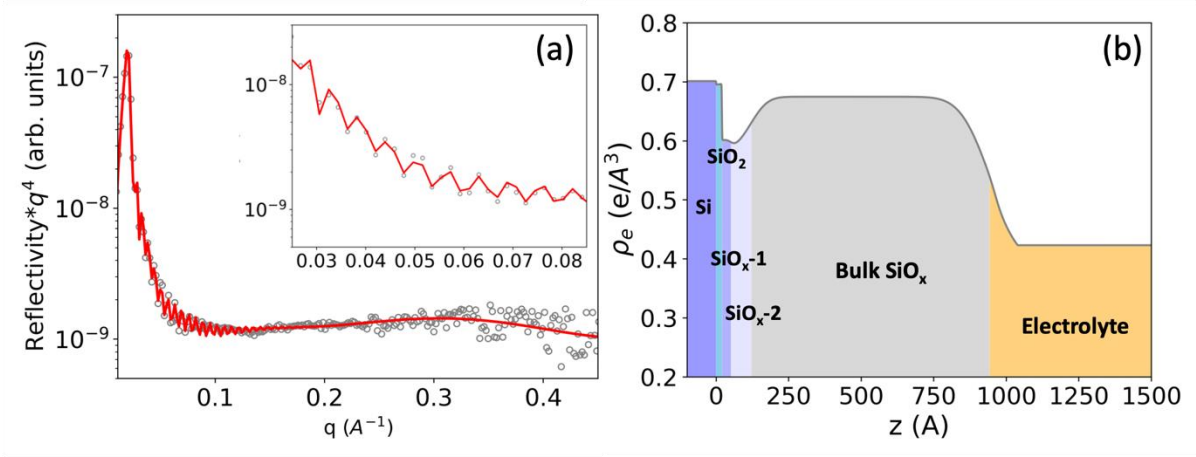

Figure 7. (a) Experimental (grey dots) and simulated (red line) XRR data (the inset is a zoom to the low-q region) and (b) the fit-derived electron density profile (EDP) of SiO_x electrode in EC/DMC based electrolyte at open circuit voltage (OCV).

The XRR fitting models evolve during the lithiation process due to changes at the electrode/electrolyte interface. For the EC/DMC-based electrolyte, a SEI layer, denoted as "L1" layer, is incorporated into the fitting model from 0.5 V vs Li^+/Li. Starting at 0.15 V vs Li^+/Li, as the electrode lithiation progresses, a single bulk SiO_x layer is not sufficient to describe the electron density gradient in the electrode due to the lithiation. Consequently, two lithiated SiO_x layers, denoted as "L2" and "L3" respectively, are used to describe the previous bulk SiO_x layer. Additionally, the SiO_2 layer is also divided into two distinct layers, denoted as "SiO_2-1" and "SiO_2-2". A schematic representation of this modified fitting model and its corresponding EDP are presented in Figure 8 (a) and (b), respectively, with detailed justifications provided in the supporting information.

In the case of the EC/DMC/FEC-based electrolyte, a SEI layer, denoted as "L1", is introduced into the fitting model from 1 V vs Li^+/Li. Beginning from 0.15 V vs Li^+/Li,

similarly to the EC/DMC-based electrolyte, the bulk SiO_x is also replaced by two lithiated SiO_x layers, denoted as "L2" and "L3". However, as for the SiO_2 layer, a single layer is sufficient for the fitting. Figure 8 (c) and (d) depict the schematic representation and the corresponding EDP for this specific case.

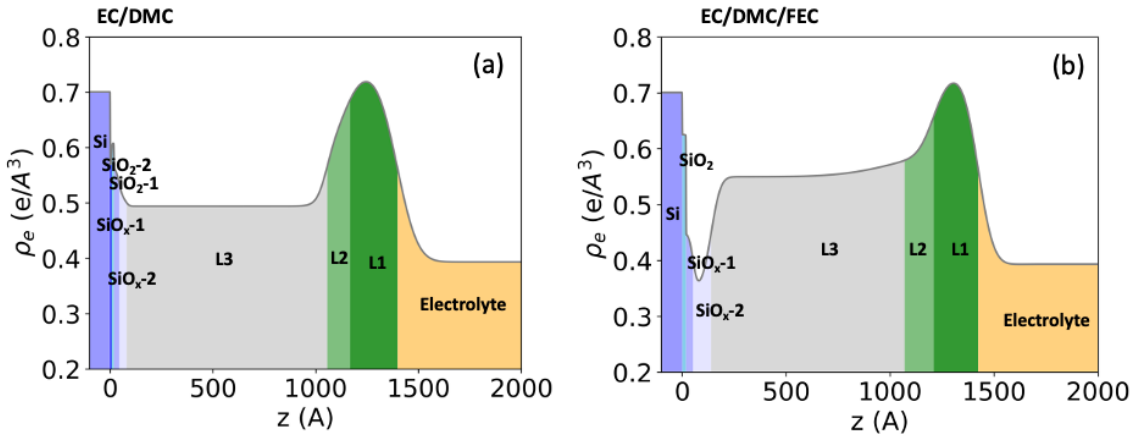

Figure 8. Schematic illustrations of XRR fitting models at the 0.15 V vs Li^+/Li of (a) EC/DMC based, (b) EC/DMC/FEC based electrolytes and the corresponding fit-derived electron density profiles. In the fitting model of the EC/DMC-based sample, the SiO_2 layer is divided into two lithiated SiO_2 layers (labeled as SiO_2-1 and SiO_2-2) due to the lithiation of SiO_2. The rationalization of this fitting model is detailed in the supporting information.

3.2.2 Qualitative analysis of XRR data

Figure 9 and Figure 10 depict normalized *operando* XRR data, both measured and simulated, along with fit-derived EDPs and the electrochemical data of SiO_x electrodes. Each of these figures is divided into three sub-figures, showing (a) the XRR data, (b) the corresponding EDPs obtained from fitting, and (c) the experimental electrochemical data. At the OCV, both datasets were analyzed using a four-layer model, as previously mentioned. The fitting models are adapted as the lithiation process progresses as described in section 3.2.1 and Figure 7.

Electrode cycled in EC/DMC based electrolyte

For the EC/DMC dataset, no evolution of the XRR profile is observed until 0.5 V vs Li^+/Li (Figure 9). At 0.5 V, Kiessig fringes of the XRR curve have a lower amplitude compared to that at 1 V vs Li^+/Li, revealing the blurring of the bulk SiO_x/electrolyte interface, suggesting the onset of a solid electrolyte interphase (SEI) formation. Therefore, the corresponding SEI layer (L1) is introduced into the fitting model. At 0.3 V vs Li^+/Li, the fit-derived EDP shows that both the thickness and electron density of the SEI increase. At 0.15 V, the raw XRR signal shows a drastic change (Figure 9 (a)) and it was found out

that the SiOx phase is split into two layers (Figure 9 (b)). The first layer, L2, located at the interface with electrolyte shows a relatively high electron density, while the second layer, L3, adjacent to the substrate, shows a significant decrease of electron density due to the lithiation. This phase segregation remains below 0.15 V and even after the delithiation process. It is noted that the thickness of the electrode layers (L2 and L3) decreases during the delithiation. The XRR curve does not change much while the SiO_x potential is kept at 2 V vs Li^+/Li, suggesting that the delithiation process is completed before this potential.

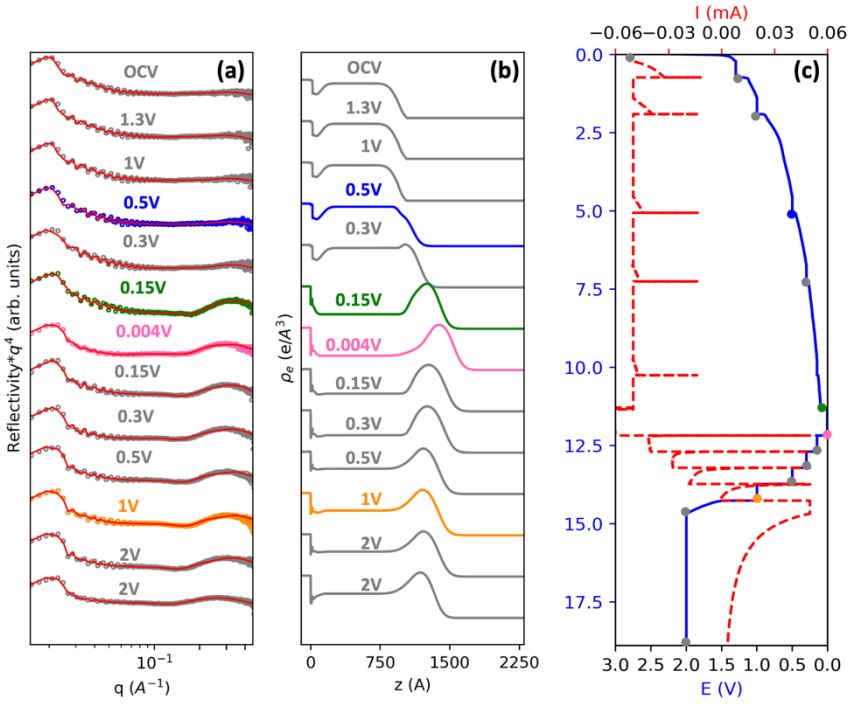

Figure 9. The first cycle of SiO_x in EC/DMC based electrolyte: (a) Experimental (dots) and fitted (lines) log-log XRR data of SiO_x at different lithiation and delithiation stages, (b) the corresponding best fit-derived electron density profiles and (c) the corresponding electrochemical data.

Electrode cycled in EC/DMC/FEC based electrolyte

The XRR curves recorded using EC/DMC/FEC between OCV and 1.3 V vs Li^+/Li do not show any change (Figure 10). From 1 V to 0.5 V vs Li^+/Li, the slope around q = 0.04 $Å^{-1}$ becomes steeper, indicating the increase of interface roughness or the formation of a rough SEI. Hence, a layer above the bulk SiO_x labeled as "L1" is introduced to the fitting model from 1 V. From 0.3 V to 0.1 V vs Li^+/Li, the fit-derived EDPs shows the densification and growth of SEI. Simultaneously, the density of the bulk SiO_x drops while the thickness increases, indicating the lithiation of SiO_x. During delithiation, the bulk SiO_x

shrinks with a gradual increase of electron density. Concurrently, a decrease of SEI thickness is observed as well. No change in the SEI or bulk SiO_x is observed at the 2 V vs Li^+/Li plateau.

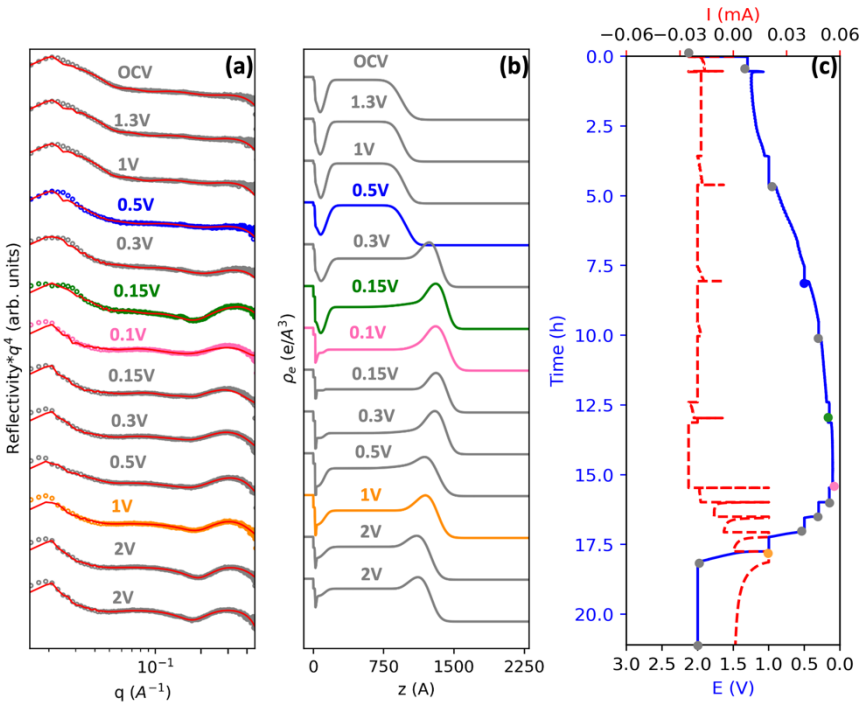

Figure 10. The first cycle of SiO_x in EC/DMC/FEC based electrolyte: (a) Experimental (dots) and fitted (lines) log-log XRR data of SiOx at different lithiation and delithiation stages, (b) the corresponding best fit-derived electron density profiles and (c) the corresponding electrochemistry. All potentials are given vs Li^+/Li.

3.2.3 Quantitative fitting results of XRR data

In this section, we will discuss the quantitative fitting results of XRR for three key layers: L1, L2 and L3. It was found out that the XRR results can be reasonably explained by assuming that L1 represents the SEI while L2 and L3 correspond to lithiated bulk SiO_x.

Electrode cycled in EC/DMC based electrolyte

Figure 11 provides a concise summary of the quantitative fitting results for three main layers observed during cycling in the EC/DMC based electrolyte: L1, L2 and L3. Figure 11 (a)-(d) show respectively the thickness, the electron density, roughness and the density-thickness product of the L1 layer while Figure 11 (l) shows the corresponding voltage of each measurement. Specifically, the density-thickness product of the layers during cycling are plotted, which unveils the electron content of the layer. This parameter is more reliable for tracking the dynamics of the target layer compared to using a single fitting parameter, such as thickness or electron density.

L1 layer (SEI)

The results show that the SEI forms at 0.5 V vs Li^+/Li with a thickness of 154 Å and a density of 0.63 $e \cdot Å^{-3}$. It is worth noting that the SEI consists of two sub-regions, an inner inorganic SEI which is adjacent to the electrode and an outer porous organic SEI[33,50]. Since the organic components have a similar electron density to that of the electrolyte, XRR is usually more sensitive to the inorganic region where the electron density is higher. Given that the electron density of LiF is 0.74 $e \cdot Å^{-3}$, the SEI at this voltage likely comprises LiF with other organic components. As the voltage decreases from 0.5 to 0.004 V vs Li^+/Li, the SEI thickness consistently increases to 274 Å, accompanied with a rise in electron density to 0.74 $e \cdot Å^{-3}$. These findings align with XPS analysis, which supports the presence of LiF and carbonate components in the SEI layer. During the delithiation process, we observe a partial dissolution of the SEI, as its thickness decreases to 247 Å while maintaining an electron density of 0.74 $e \cdot Å^{-3}$. This suggests the persistent dominance of LiF in the (inorganic) SEI composition, as corroborated by XPS spectra at 0.8 V vs Li^+/Li during delithiation indicating the presence of LiF and free carbonate organic components. Furthermore, the density-thickness product of the SEI, which reveals the electron content of the layer, shows a similar trend to that of SEI thickness. The roughness of SEI fluctuates between 70 Å and 87 Å during the cycling.

L2 layer (bulk $SiO_x \rightarrow Li_xSi_y$ and Li_zSiO_t)

As mentioned previously, the lithiation of the bulk SiO_x increases the electron density gradient with the electrode. In the previous fitting model, L3, which has a uniform electron density and was located just below L1 (SEI), was the only layer used to describe the bulk SiO_x layer from OCV to 0.3 V vs Li^+/Li. However, starting from 0.15 V, the phase gradation within bulk SiO_x necessitates a refined approach. In the modified fitting model, both L2 and L3 are introduced to better describe the lithiated bulk SiO_x layer.

The thickness, electron density, roughness and density-thickness product of the L2 layer are depicted in Figure 11 (e)-(h). As lithiation progresses, from 0.15 V to 0.004 V vs Li^+/Li, the thickness of L2 exhibits a slight increase from 110 Å to 192 Å, followed by a gradual decrease to 82 Å during the delithiation. The electron density concurrently decreases from 0.63 $e \cdot Å^{-3}$ to 0.56 $e \cdot Å^{-3}$ during lithiation and gradually rebounds to 0.7 $e \cdot Å^{-3}$ during delithiation. The roughness of this layer varies between 45 Å and 70 Å during the cycling.

L3 layer (bulk SiO_x → Li_xSi_y and Li_zSiO_t)

The evolution of the thickness, the electron density and the roughness of L3 layer are illustrated in Figure 11 (i)-(k). In Figure 11 (i), the grey dots indicate the thickness of the L3 layer while the black dots represent the total thickness of the lithiated bulk SiO_x layer (L2 + L3). The thickness and the density of the L3 layer remain constant from OCV to 0.5 V vs Li^+/Li, indicating that the lithiation of bulk SiO_x begins at a voltage lower than 0.5 V. From 0.5 V to 0.3 V vs Li^+/Li, the thickness of L3 increases gradually from 823 Å to 867 Å, suggesting the onset of SiO_x lithiation. From 0.15 V vs Li^+/Li, the lithiated bulk SiO_x is represented by both L2 and L3 layers. During lithiation, both the L3 thickness and the total thickness of L2 and L3 increase, reaching maximum values of 1001 Å and 1193 Å respectively. Concurrently, the electron density of L3 decreases to 0.5 $e \cdot Å^{-3}$. This lower density indicates that the compositions of L3 layer comprises Li_zSiO_t along with other low-density compounds, such as Li_xSi_y and amorphous Li_zSiO_t. During delithiation, both the L3 thickness and the total bulk SiO_x thickness gradually decrease. The L3 thickness returns to 926 Å, while the total bulk SiO_x thickness returns to 1008 Å. The results reveal a breathing behavior of bulk SiO_x during the cycling process. Meanwhile, the electron density of L3 increases back to 0.57 $e \cdot Å^{-3}$ at the end of the delithiation, which is lower than the initial electron density of the bulk SiO_x layer, suggesting the presence of irreversible lithiated products.

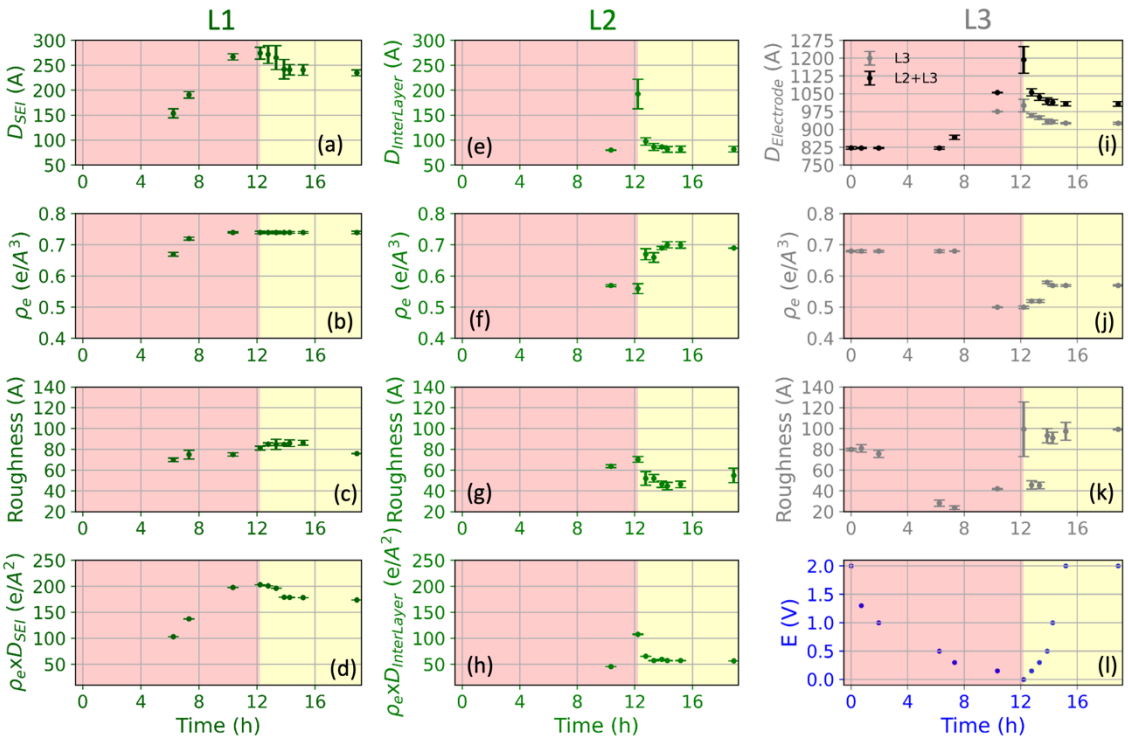

Figure 11. XRR fit-derived quantitative results of the sample cycled in EC/DMC based electrolyte: (a)-(d) Thickness, electron density, roughness and electron density-thickness product of L1 layer; (e)-(h) Thickness, electron density, roughness and electron density-thickness product of L2 layer;(i)-(k) Thickness, electron density and roughness of L3 layer; Black dots represent the total thickness of bulk SiO_x. (l) The corresponding voltages vs Li^+/Li of each XRR dataset.

Electrode cycled in EC/DMC/FEC based electrolyte

The quantitative fitting results of the EC/DMC/FEC cell are summarized in Figure 12.

L1 layer (SEI)

In Figure 12 (a)-(d), we present respectively the thickness, the electron density, roughness and the density-thickness product of the L1 (SEI) layer while Figure 12 (l) corresponds to the voltages for each XRR dataset. It is known from the literature that FEC undergoes reductive decomposition at a voltage higher than 1 V vs Li^+/Li to form an initial SEI on the Si-based electrode[27,28]. As a result, we introduce the L1 layer, representing the SEI layer, into the XRR fitting model starting from 1 V. Initially, at 1 V, the L1 layer exhibits a thickness of 75 Å with a density of 0.44 $e \cdot Å^{-3}$ and a roughness of 50 Å. This low density, close to that of the electrolyte, along with the high roughness, suggests that at this voltage, the SEI layer is not yet well-constructed and is primarily composed of organic species. This finding aligns with the XPS results. As the voltage drops to 0.3 V vs Li^+/Li, the thickness of the SEI increases rapidly to 205 Å, and its electron density increases to 0.74 $e \cdot Å^{-3}$ during lithiation. This high electron density indicates that the L1 layer is

predominantly composed of LiF at this voltage. In connection with the previous *ex situ* XPS results, we interpret these findings as indicating the formation of a well-defined solid electrolyte interphase (SEI) at 0.3 V vs Li^+/Li in the EC/DMC/FEC-based electrolyte. From 0.3 V to 0.1 V vs Li^+/Li, L1 experiences a slight growth to 218 Å, with an electron density remaining at 0.74 $e \cdot Å^{-3}$. During delithiation, L1 demonstrates a breathing behavior as its thickness shrinks to 185 Å, while its density remains around 0.74 $e \cdot Å^{-3}$, showing good stability during the delithiation process. Additionally, the roughness of L1 varies from 50 Å to 90 Å during the cycling process.

L2 layer (bulk $SiO_x \rightarrow Li_xSi_y$ and Li_zSiO_t)

Similar to the EC/DMC system, we found out that including a L2 layer is not necessary down to 0.3V in order to fit the raw XRR signal, but should be included after 0.3V to obtain a precise fit. Quantitative fitting results of the L2 layer are shown in Figure 12 (e)-(h). From the emergence of the L2 layer at 0.15 V vs Li^+/Li in lithiation stage until the start of delithiation at 0.3 V, L2 maintains stability in both thickness and electron density, with a thickness around 140 Å and an electron density around 0.6 $e \cdot Å^{-3}$. During the further delithiation process, L2 gradually shrinks to 94 Å, accompanied by a progressive increase of electron density to 0.68 $e \cdot Å^{-3}$.

L3 layer (bulk $SiO_x \rightarrow Li_xSi_y$ and Li_zSiO_t)

The quantitative fitting results of the L3 layer in the EC/DMC/FEC system are summarized in Figure 12 (i)-(k). Like what was observed in the EC/DMC system, from OCV to 0.5 V vs Li^+/Li, L3 represents the total bulk SiO_x layer and exhibits no evolution in thickness or electron density. However, from 0.3 V, the thickness of the bulk SiO_x layer increases from 815 Å to 1000 Å accompanied by a drop in electron density from 0.68 to 0.6 $e \cdot Å^{-3}$. Starting from 0.15 V, the bulk SiO_x layer is described by both L2 and L3 layers. In Figure 12 (i), grey dots represent the thickness evolution of L3, while black dots show the evolution of the total lithiated bulk SiO_x layer. Both thicknesses increase during lithiation, reaching maximum values of 954 Å and 1094 Å respectively. Simultaneously, the electron density of L3 drops to 0.54 $e \cdot Å^{-3}$. These results signify the lithiation of SiO_x, causing the expansion of the L3 layer. During delithiation, both the L3 thickness and the total bulk SiO_x thickness decrease. At the end of delithiation (2 V vs Li^+/Li), the L3 thickness drops to 855 Å, while the total thickness of the delithiated bulk SiO_x layer drops to 948 Å. Concurrently, the electron density of L3 rises back to 0.63 $e \cdot Å^{-3}$. While slightly

higher than the 0.57 e·Å^{-3} observed in the EC/DMC system, it remains lower than the initial electron density of the bulk SiO_x layer, suggesting the presence of some irreversible compounds within the L3 layer after delithiation.

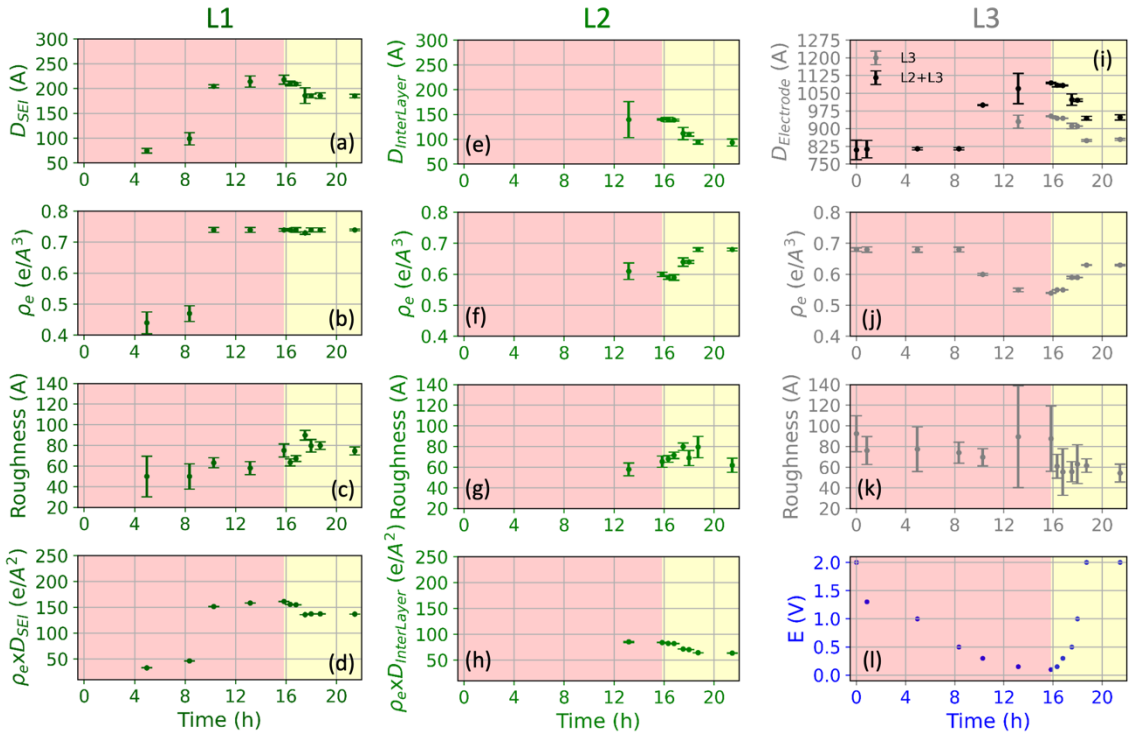

Figure 12. XRR fit-derived quantitative results of the sample cycled in EC/DMC/FEC based electrolyte: (a)-(d) Thickness, electron density, roughness and electron density-thickness product of the L1 layer. (e)-(h) Thickness, electron density, roughness and electron density-thickness product of the L2 layer. (i)-(k) Thickness, electron density and roughness of the L3 layer; black dots represent the total thickness of bulk SiO_x. (l) The corresponding voltages vs Li^+/Li of each XRR dataset.

3.2.4 Comparison between different electrolytes and discussion

The quantitative fitting results of the L1, L2 and L3 layers for the EC/DMC and EC/DMC/FEC systems reveal some similarities and differences in the evolution of the SiO_x surface during cycling.

In both EC/DMC and EC/DMC/FEC systems, the SEI and bulk SiO_x layers exhibit a breathing behavior, growing during lithiation and partially dissolving during delithiation, indicating common structural dynamics. However, notable differences emerge: the SEI thickness in EC/DMC (reaching 274 Å) surpasses that in EC/DMC/FEC (peaking at 218 Å), suggesting that FEC influences SEI layer growth. In addition, the density-thickness product suggests that the SEI is more stable in EC/DMC/FEC. This is because the density-thickness product is an indicator of the electron content within the layer, and its values vary

less in EC/DMC/FEC, indicating that the reactions are more modest in this FEC containing system.

3.3 (De)lithiation model/SEI model

In this section, we integrate the insights from *ex situ* XPS analysis and *operando* XRR analysis to provide a comprehensive description of the SiO_x thin film evolution during lithiation/delithiation. Figure 13 summarizes the surface evolution of the SiO_x electrode during cycling. Initially, the *ex situ* XPS analysis reveals that, for both electrolytes, no significant changes in the SiO_x electrode thickness or Si 2p spectra occur before 0.4 V vs Li^+/Li, suggesting the beginning of SiO_x lithiation after this voltage. Furthermore, no significant signals of SEI are detected before 0.4 V. At 0.4 V, LiF signals are detected in both electrolytes. This indicates an intimate relationship between the formation of SEI and the lithiation of the SiO_x electrode, a notion corroborated by *operando* XRR results. Indeed, *operando* XRR results confirm that, for both electrolytes, the electron density and the thickness of the bulk SiO_x layer only start evolving from 0.3 V vs Li^+/Li, affirming the initiation of SiO_x lithiation below 0.4 V vs Li^+/Li. In the FEC containing system, the thickness of L1 layer significantly increases between 0.3 and 0.5 V although the L1 layer was introduced already at 1 V vs Li^+/Li (Figure 12(a)). In the FEC free system, the L1 layer starts to grow around 0.5 V (Figure 11(a)).

This observation suggests that the additional FEC did not form a SEI prior to the decomposition of EC. We hypothesize that the delayed decomposition of FEC is due to the high resistivity of SiO_x that restricts electron transport from the electrode to the electrode/electrolyte interface. This hypothesis aligns with the findings of Steinrück *et al.* in their investigation of the lithiation of native oxide-terminated Si[51]. In their study, they observed that the formation of SEI and LiF starts only after the lithiation of the native oxide layer. This layer, characterized by a high resistivity, serves as a protective barrier, expanding the electrochemical stability window of electrolytes down to 0.7 V vs Li^+/Li[51].

In addition, *ex situ* XPS reveals a thickness expansion of SiO_x during lithiation and a shrinkage during delithiation for both electrolytes. *Operando* XRR confirms this "breathing behavior", indicating that the addition of FEC does not significantly affect the lithiation of SiO_x. Regarding chemical compositions, *ex situ* XPS reports the evolution of

the electrode's chemical composition from SiO_x to Li_zSiO_t and Li_xSi_y during lithiation, and these compositions remain unchanged during delithiation, indicating irreversibility. This is further supported by *operando* XRR results, that detail the lithiation-induced transformation of the initial bulk SiO_x layer into two lithiated layers (L2 and L3), with L2 mainly consisting of Li_zSiO_t located close to the surface and L3 primarily composed of Li_xSi_y below.

Regarding SEI evolution, *ex situ* XPS finds similar chemical compositions of the SEI in both FEC-containing and FEC-free electrolytes. For example, LiF is the main component in L1 (top-SEI) layer for both systems, and Li_2CO_3 is found only at 0.01 V and disappears during the delithiation. However, the SEI formed in the FEC-containing electrolyte exhibits a lower thickness both at the end of lithiation and at the end of delithiation. Additionally, for both electrolytes, *ex situ* XPS observes a partial dissolution of the SEI, findings further validated by *operando* XRR results. The XRR results track SEI evolution during cycling, revealing that, at the end of lithiation, the FEC-containing system results in a thinner SEI (218 Å) compared to the FEC-free system (274 Å). Moreover, regardless of FEC presence, the SEI undergoes partial dissolution during delithiation, as seen in the XPS and XRR results.

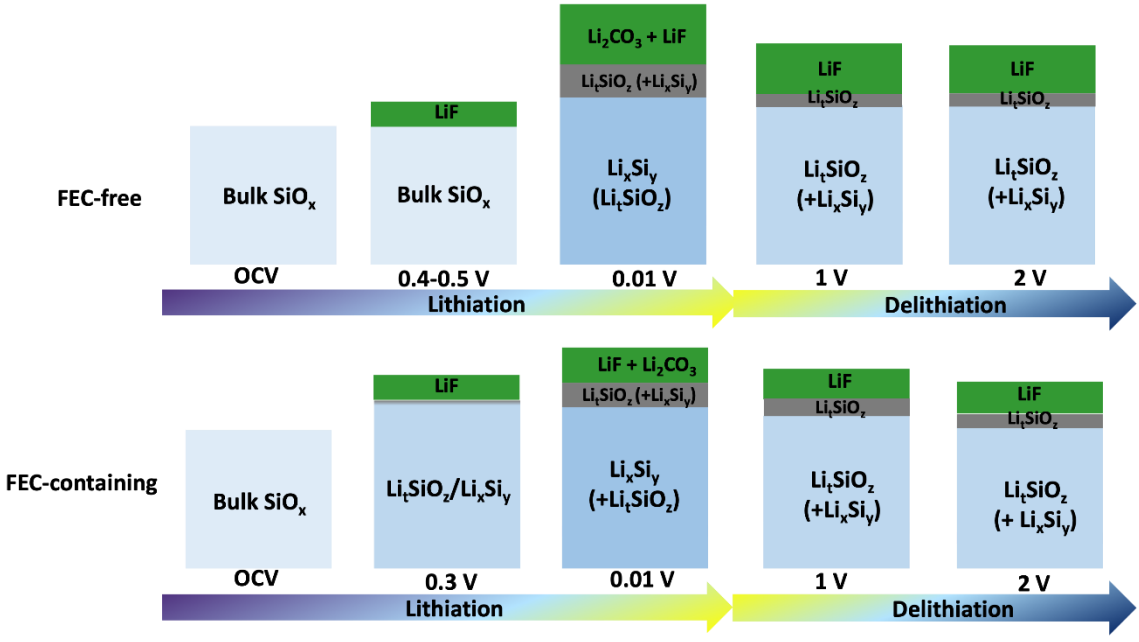

Figure 13. Schematic summary of SiO_x thin film surface evolution during cycling. Note that the organic SEI is omitted. Voltages are referred vs Li^+/Li. The color of bulk SiO_x phases qualitatively reflects its electron density.

4. Conclusion

In conclusion, we have provided the first combined *ex situ* XPS and *operando* XRR study of SiO_x thin film electrodes, allowing to probe both the chemistry and the thickness evolution of the SEI and the active material. This study provides a thorough investigation into the dynamic evolution of SiO_x thin film electrodes during the first lithiation/delithiation cycle. We obtain a combined view of local atomic environments and electronic density variation through the thickness of the SEI and of the bulk material. We find that the SEI is mainly composed of LiF and lithium carbonates, of different proportion depending on the electrolyte composition. The integrated insights unveil that SiO_x lithiation initiates below 0.4 V vs Li^+/Li, with an intimate correlation between SEI formation and SiO_x electrode lithiation. Despite similar SEI chemical components in FEC-containing and FEC-free electrolytes, the former displays a thinner SEI. In the lithiation process, both the SEI and the SiO_x thicken. In the delithiation process, the SiO_x becomes thinner as expected, but its final thickness is larger than that of pristine sample. Chemical composition analysis underscore irreversible lithiation processes, transitioning from SiO_x to Li_zSiO_t and Li_xSi_y. It was also found out that the thickness of the SEI decreases during delithiation for both electrolyte compositions, which may be due to a partial dissolution of the SEI. These observations provide valuable insights into the understanding of electrode lithiation and surface evolution during the early formation cycles of SiO_x, a material currently being considered for next-generation lithium-ion batteries at the industrial level.

Supporting information: Si 2p core level spectrum of the pristine SiO_x thin film, Sputtering time of Si-free layer formed on the electrode surface after cycling, Si atomic concentration relative to the oxidation states of silicon atoms, XPS depth profiling spectra of C 1s, F 1s, O 1s and P 2p core levels of SiO_x thin films electrodes cycled in EC/DMC and FEC/DMC, XPS quantification of SEI composition depending on the electrolyte, Rationalization of XRR fitting models for the pristine electrode, Electron density profiles of pristine electrodes in different electrolytes, Rationalization of XRR fitting models for the EC/DMC cell, SEM images of the cross-section of SiO_x thin film are supplied as Supporting information.

5. References

(1) Nagaura, T. Lithium Ion Rechargeable Battery. *Progress in Batteries & Solar Cells* **1990**, *9*, 209.

(2) Thackeray, M. M.; Wolverton, C.; Isaacs, E. D. Electrical Energy Storage for Transportation—Approaching the Limits of, and Going beyond, Lithium-Ion Batteries. *Energy Environ Sci* **2012**, *5* (7), 7854–7863.

(3) Beaulieu, L. Y.; Eberman, K. W.; Turner, R. L.; Krause, L. J.; Dahn, J. R. Colossal Reversible Volume Changes in Lithium Alloys. *Electrochemical and Solid-State Letters* **2001**, *4* (9), A137.

(4) Kasavajjula, U.; Wang, C.; Appleby, A. J. Nano-and Bulk-Silicon-Based Insertion Anodes for Lithium-Ion Secondary Cells. *J Power Sources* **2007**, *163* (2), 1003–1039.

(5) Obrovac, M. N.; Christensen, L. Structural Changes in Silicon Anodes during Lithium Insertion/Extraction. *Electrochemical and solid-state letters* **2004**, *7* (5), A93.

(6) Li, H.; Huang, X.; Chen, L.; Wu, Z.; Liang, Y. A High Capacity Nano Si Composite Anode Material for Lithium Rechargeable Batteries. *Electrochemical and solid-state letters* **1999**, *2* (11), 547.

(7) Obrovac, M. N.; Krause, L. J. Reversible Cycling of Crystalline Silicon Powder. *J Electrochem Soc* **2006**, *154* (2), A103.

(8) Chen, T.; Wu, J.; Zhang, Q.; Su, X. Recent Advancement of SiOx Based Anodes for Lithium-Ion Batteries. *J Power Sources* **2017**, *363*, 126–144.

(9) Hsu, C.-H.; Chen, H.-Y.; Tsai, C.-J. Stoichiometry Dependence of Electrochemical Behavior of Silicon Oxide Thin Film for Lithium Ion Batteries. *J Power Sources* **2019**, *438*, 226943.

(10) Sitinamaluwa, H. S.; Li, H.; Wasalathilake, K. C.; Wolff, A.; Tesfamichael, T.; Zhang, S.; Yan, C. Nanoporous SiOx Coated Amorphous Silicon Anode Material with Robust Mechanical Behavior for High-Performance Rechargeable Li-Ion Batteries. *Nano Materials Science* **2019**, *1* (1), 70–76.

(11) Wu, H.; Chan, G.; Choi, J. W.; Ryu, I.; Yao, Y.; McDowell, M. T.; Lee, S. W.; Jackson, A.; Yang, Y.; Hu, L. Stable Cycling of Double-Walled Silicon Nanotube Battery Anodes through Solid–Electrolyte Interphase Control. *Nat Nanotechnol* **2012**, *7* (5), 310–315.

(12) Liu, Q.; Cui, Z.; Zou, R.; Zhang, J.; Xu, K.; Hu, J. Surface Coating Constraint Induced Anisotropic Swelling of Silicon in Si–Void@ SiO x Nanowire Anode for Lithium-ion Batteries. *Small* **2017**, *13* (13), 1603754.

(13) Tao, H.-C.; Huang, M.; Fan, L.-Z.; Qu, X. Interweaved Si@ SiOx/C Nanoporous Spheres as Anode Materials for Li-Ion Batteries. *Solid State Ion* **2012**, *220*, 1–6.

(14) Goriparti, S.; Miele, E.; De Angelis, F.; Di Fabrizio, E.; Zaccaria, R. P.; Capiglia, C. Review on Recent Progress of Nanostructured Anode Materials for Li-Ion Batteries. *J Power Sources* **2014**, *257*, 421–443.

(15) Adnan, S.; Mohamed, N. S. Citrate Sol–Gel Synthesised Li4SiO4: Conductivity and Dielectric Behaviour. *Materials Research Innovations* **2012**, *16* (4), 281–285.

(16) Jung, S. C.; Kim, H.-J.; Kim, J.-H.; Han, Y.-K. Atomic-Level Understanding toward a High-Capacity and High-Power Silicon Oxide (SiO) Material. *The Journal of Physical Chemistry C* **2015**, *120* (2), 886–892.

(17) Li, H.; Li, H.; Yang, Z.; Yang, L.; Gong, J.; Liu, Y.; Wang, G.; Zheng, Z.; Zhong, B.; Song, Y. SiOx Anode: From Fundamental Mechanism toward Industrial Application. *Small* **2021**, *17* (51), 2102641.

(18) Zhu, X.; Liu, B.; Shao, J.; Zhang, Q.; Wan, Y.; Zhong, C.; Lu, J. Fundamental Mechanisms and Promising Strategies for the Industrial Application of SiOx Anode. *Adv Funct Mater* **2023**, *33* (17), 2213363.

(19) Xiao, H.; Fang, C.; Zheng, T.; Bai, H.; Liu, G. Investigation of SiOx Anode Fading Mechanism with Limited Capacity Cycling. *APL Mater* **2022**, *10* (1), 011108.

(20) Takezawa, H.; Ito, S.; Yoshizawa, H.; Abe, T. Surface Composition of a SiOx Film Anode Cycled in Carbonate Electrolyte for Li-Ion Batteries. *Electrochim Acta* **2017**, *229*, 438–444.

(21) Li, Z.; Jin, J.; Yuan, Z.; Yang, W. Surface Modification of SiOx Film Anodes by Laser Annealing and Improvement of Cyclability for Lithium-Ion Batteries. *Mater Sci Semicond Process* **2021**, *121*, 105300.

(22) Guo, K.; Kumar, R.; Xiao, X.; Sheldon, B. W.; Gao, H. Failure Progression in the Solid Electrolyte Interphase (SEI) on Silicon Electrodes. *Nano Energy* **2020**, *68*, 104257.

(23) Peled, E.; Menkin, S. SEI: Past, Present and Future. *J Electrochem Soc* **2017**, *164* (7), A1703.

(24) Aurbach, D.; Gamolsky, K.; Markovsky, B.; Gofer, Y.; Schmidt, M.; Heider, U. On the Use of Vinylene Carbonate (VC) as an Additive to Electrolyte Solutions for Li-Ion Batteries. *Electrochim Acta* **2002**, *47* (9), 1423–1439.

(25) Nie, M.; Demeaux, J.; Young, B. T.; Heskett, D. R.; Chen, Y.; Bose, A.; Woicik, J. C.; Lucht, B. L. Effect of Vinylene Carbonate and Fluoroethylene Carbonate on SEI Formation on Graphitic Anodes in Li-Ion Batteries. *J Electrochem Soc* **2015**, *162* (13), A7008.

(26) Jin, Y.; Kneusels, N.-J. H.; Marbella, L. E.; Castillo-Martínez, E.; Magusin, P. C. M. M.; Weatherup, R. S.; Jónsson, E.; Liu, T.; Paul, S.; Grey, C. P. Understanding Fluoroethylene Carbonate and Vinylene Carbonate Based Electrolytes for Si Anodes in Lithium Ion Batteries with NMR Spectroscopy. *J Am Chem Soc* **2018**, *140* (31), 9854–9867.

(27) Xu, C.; Lindgren, F.; Philippe, B.; Gorgoi, M.; Bjorefors, F.; Edstrom, K.; Gustafsson, T. Improved Performance of the Silicon Anode for Li-Ion Batteries: Understanding the Surface Modification Mechanism of Fluoroethylene Carbonate as an Effective Electrolyte Additive. *Chemistry of Materials* **2015**, *27* (7), 2591–2599.

(28) Veith, G. M.; Doucet, M.; Sacci, R. L.; Vacaliuc, B.; Baldwin, J. K.; Browning, J. F. Determination of the Solid Electrolyte Interphase Structure Grown on a Silicon Electrode Using a Fluoroethylene Carbonate Additive. *Sci Rep* **2017**, *7* (1), 6326.

(29) Somerville, L.; Bareño, J.; Jennings, P.; McGordon, A.; Lyness, C.; Bloom, I. The Effect of Pre-Analysis Washing on the Surface Film of Graphite Electrodes. *Electrochim Acta* **2016**, *206*, 70–76.

(30) Waldmann, T.; Iturrondobeitia, A.; Kasper, M.; Ghanbari, N.; Aguesse, F.; Bekaert, E.; Daniel, L.; Genies, S.; Gordon, I. J.; Löble, M. W. Post-Mortem Analysis of Aged Lithium-Ion Batteries: Disassembly Methodology and Physico-Chemical Analysis Techniques. *J Electrochem Soc* **2016**, *163* (10), A2149.

(31) Cao, C.; Steinrück, H.-G.; Shyam, B.; Stone, K. H.; Toney, M. F. In Situ Study of Silicon Electrode Lithiation with X-Ray Reflectivity. *Nano Lett* **2016**, *16* (12), 7394–7401.

(32) Cao, C.; Steinrück, H.; Shyam, B.; Toney, M. F. The Atomic Scale Electrochemical Lithiation and Delithiation Process of Silicon. *Adv Mater Interfaces* **2017**, *4* (22), 1700771.

(33) Cao, C.; Abate, I. I.; Sivonxay, E.; Shyam, B.; Jia, C.; Moritz, B.; Devereaux, T. P.; Persson, K. A.; Steinrück, H.-G.; Toney, M. F. Solid Electrolyte Interphase on Native Oxide-Terminated Silicon Anodes for Li-Ion Batteries. *Joule* **2019**, *3* (3), 762–781.

(34) Jerliu, B.; Huger, E.; Dorrer, L.; Seidlhofer, B.-K.; Steitz, R.; Oberst, V.; Geckle, U.; Bruns, M.; Schmidt, H. Volume Expansion during Lithiation of Amorphous Silicon Thin Film Electrodes Studied by In-Operando Neutron Reflectometry. *The Journal of Physical Chemistry C* **2014**, *118* (18), 9395–9399.

(35) Phan, V. P.; Pecquenard, B.; Le Cras, F. High-performance All-solid-state Cells Fabricated with Silicon Electrodes. *Adv Funct Mater* **2012**, *22* (12), 2580–2584.

(36) Tomozeiu, N. Electrical Conduction and Dielectric Relaxation of A-SiOx (0< X< 2) Thin Films Deposited by Reactive RF Magnetron Sputtering. *Thin Solid Films* **2008**, *516* (22), 8199–8204.

(37) van Hapert, J. J. Hopping Conduction and Chemical Structure- a Study on Silicon Suboxides. *PhD Thesis Utrecht University* **2002**.

(38) Reynier, Y.; Vincens, C.; Leys, C.; Amestoy, B.; Mayousse, E.; Chavillon, B.; Blanc, L.; Gutel, E.; Porcher, W.; Hirose, T. Practical Implementation of Li Doped SiO in High Energy Density 21700 Cell. *J Power Sources* **2020**, *450*, 227699.

(39) Su, Y.-S.; Hsiao, K.-C.; Sireesha, P.; Huang, J.-Y. Lithium Silicates in Anode Materials for Li-Ion and Li Metal Batteries. *Batteries* **2022**, *8* (1), 2.

(40) Philippe, B.; Dedryvère, R.; Gorgoi, M.; Rensmo, H.; Gonbeau, D.; Edström, K. Improved Performances of Nanosilicon Electrodes Using the Salt LiFSI: A Photoelectron Spectroscopy Study. *J Am Chem Soc* **2013**, *135* (26), 9829–9842.

(41) Radvanyi, E.; De Vito, E.; Porcher, W.; Larbi, S. J. S. An XPS/AES Comparative Study of the Surface Behaviour of Nano-Silicon Anodes for Li-Ion Batteries. *J Anal At Spectrom* **2014**, *29* (6), 1120–1131.

(42) Younesi, R.; Hahlin, M.; Edström, K. Surface Characterization of the Carbon Cathode and the Lithium Anode of Li–O2 Batteries Using LiClO4 or LiBOB Salts. *ACS Appl Mater Interfaces* **2013**, *5* (4), 1333–1341.

(43) Young, B. T.; Heskett, D. R.; Nguyen, C. C.; Nie, M.; Woicik, J. C.; Lucht, B. L. Hard X-Ray Photoelectron Spectroscopy (HAXPES) Investigation of the Silicon Solid Electrolyte Interphase (SEI) in Lithium-Ion Batteries. *ACS Appl Mater Interfaces* **2015**, *7* (36), 20004–20011.

(44) Philippe, B.; Dedryvère, R.; Allouche, J.; Lindgren, F.; Gorgoi, M.; Rensmo, H.; Gonbeau, D.; Edström, K. Nanosilicon Electrodes for Lithium-Ion Batteries: Interfacial Mechanisms Studied by Hard and Soft X-Ray Photoelectron Spectroscopy. *Chemistry of Materials* **2012**, *24* (6), 1107–1115.

(45) Chusid, O. Y.; Ely, E. E.; Aurbach, D.; Babai, M.; Carmeli, Y. Electrochemical and Spectroscopic Studies of Carbon Electrodes in Lithium Battery Electrolyte Systems. *J Power Sources* **1993**, *43* (1–3), 47–64.

(46) Aurbach, D.; Ein-Eli, Y.; Chusid, O.; Carmeli, Y.; Babai, M.; Yamin, H. The Correlation between the Surface Chemistry and the Performance of Li-carbon Intercalation Anodes for Rechargeable 'Rocking-Chair'Type Batteries. *J Electrochem Soc* **1994**, *141* (3), 603.

(47) El Ouatani, L.; Dedryvère, R.; Siret, C.; Biensan, P.; Gonbeau, Djj. Effect of Vinylene Carbonate Additive in Li-Ion Batteries: Comparison of LiCoO2⁄C, LiFePO4⁄C, and LiCoO2⁄Li4Ti5O12 Systems. *J Electrochem Soc* **2009**, *156* (6), A468.

(48) Chen, X.; Li, X.; Mei, D.; Feng, J.; Hu, M. Y.; Hu, J.; Engelhard, M.; Zheng, J.; Xu, W.; Xiao, J. Reduction Mechanism of Fluoroethylene Carbonate for Stable Solid–Electrolyte Interphase Film on Silicon Anode. *ChemSusChem* **2014**, *7* (2), 549–554.

(49) Hou, T.; Yang, G.; Rajput, N. N.; Self, J.; Park, S.-W.; Nanda, J.; Persson, K. A. The Influence of FEC on the Solvation Structure and Reduction Reaction of LiPF6/EC Electrolytes and Its Implication for Solid Electrolyte Interphase Formation. *Nano Energy* **2019**, *64*, 103881.

(50) Tokranov, A.; Sheldon, B. W.; Li, C.; Minne, S.; Xiao, X. In Situ Atomic Force Microscopy Study of Initial Solid Electrolyte Interphase Formation on Silicon

Electrodes for Li-Ion Batteries. *ACS Appl Mater Interfaces* **2014**, *6* (9), 6672–6686.

(51) Cao, C.; Shyam, B.; Wang, J.; Toney, M. F.; Steinrück, H.-G. Shedding X-Ray Light on the Interfacial Electrochemistry of Silicon Anodes for Li-Ion Batteries. *Acc Chem Res* **2019**, *52* (9), 2673–2683.

Table of Contents